Bone Reports 16 (2022) 101528

Contents lists available at ScienceDirect

Bone Reports

journal homepage: www.elsevier.com/locate/bonr

Growth patterns and shape development of the paediatric mandible – A 3D statistical model

Eimear O' Sullivan [a,b,d,1,*], Lara S. van de Lande [a,b,c,e,1], Khalid El Ghoul [e,1], Maarten J. Koudstaal [a,b,e], Silvia Schievano [a,b], Roman H. Khonsari [c], David J. Dunaway [a,b], Stefanos Zafeiriou [d]

[a] UCL Great Ormond Street Institute of Child Health, London, UK
[b] Craniofacial Unit, Great Ormond Street Hospital for Children, London, UK
[c] Department of Maxillofacial Surgery and Plastic Surgery, Necker - Enfants Malades University Hospital, Assistance Publique - Hôpitaux de Paris, Faculty of Medicine, University of Paris, Paris, France
[d] Department of Computing, Imperial College London, London, UK
[e] Department of Oral and Maxillofacial Surgery, Erasmus Medical Centre, Rotterdam, the Netherlands

ARTICLE INFO

Keywords:
Infant mandible
Paediatric mandible
Morphometrics
Partial least squares
3D morphable model
Statistical model

ABSTRACT

Background/aim: To develop a 3D morphable model of the normal paediatric mandible to analyse shape development and growth patterns for males and females.

Methods: Computed tomography (CT) data was collected for 242 healthy children referred for CT scan between 2011 and 2018 aged between 0 and 47 months (mean, 20.6 ± 13.4 months, 59.9% male). Thresholding techniques were used to segment the mandible from the CT scans. All mandible meshes were annotated using a defined set of 52 landmarks and processed such that all meshes followed a consistent triangulation. Following this, the mandible meshes were rigidly aligned to remove translation and rotation effects, while size effects were retained. Principal component analysis (PCA) was applied to the processed meshes to construct a generative 3D morphable model. Partial least squares (PLS) regression was also applied to the processed data to extract the shape modes with which to evaluate shape differences for age and sex. Growth curves were constructed for anthropometric measurements.

Results: A 3D morphable model of the paediatric mandible was constructed and validated with good generalisation, compactness, and specificity. Growth curves of the assessed anthropometric measurements were plotted without significant differences between male and female subjects. The first principal component was dominated by size effects and is highly correlated with age at time of scan (Spearman's $r = 0.94$, $p < 0.01$). As with PCA, the first extracted PLS mode captures much of the size variation within the dataset and is highly correlated with age (Spearman's $r = -0.94$, $p < 0.01$). Little correlation was observed between extracted shape modes and sex with either PCA or PLS for this study population.

Conclusion: The presented 3D morphable model of the paediatric mandible enables an understanding of mandibular shape development and variation by age and sex. It allowed for the construction of growth curves, which contains valuable information that can be used to enhance our understanding of various disorders that affect the mandibular development. Knowledge of shape changes in the growing mandible has potential to improve diagnostic accuracy for craniofacial conditions that impact the mandibular morphology, objective evaluation, surgical planning, and patient follow-up.

1. Introduction

Three-dimensional (3D) analysis of anatomical shape has demonstrated to be of great value and allows for many applications within the medical field. For example, face shape information can be used for diagnostic purposes or surgical planning (O'Sullivan et al., n.d.;

* Corresponding author at: UCL Great Ormond Street Institute of Child Health, London, UK.
E-mail address: e.o-sullivan16@imperial.ac.uk (E. O' Sullivan).
[1] These authors contributed equally to this work.

https://doi.org/10.1016/j.bonr.2022.101528
Received 7 January 2022; Received in revised form 25 March 2022; Accepted 28 March 2022
Available online 31 March 2022

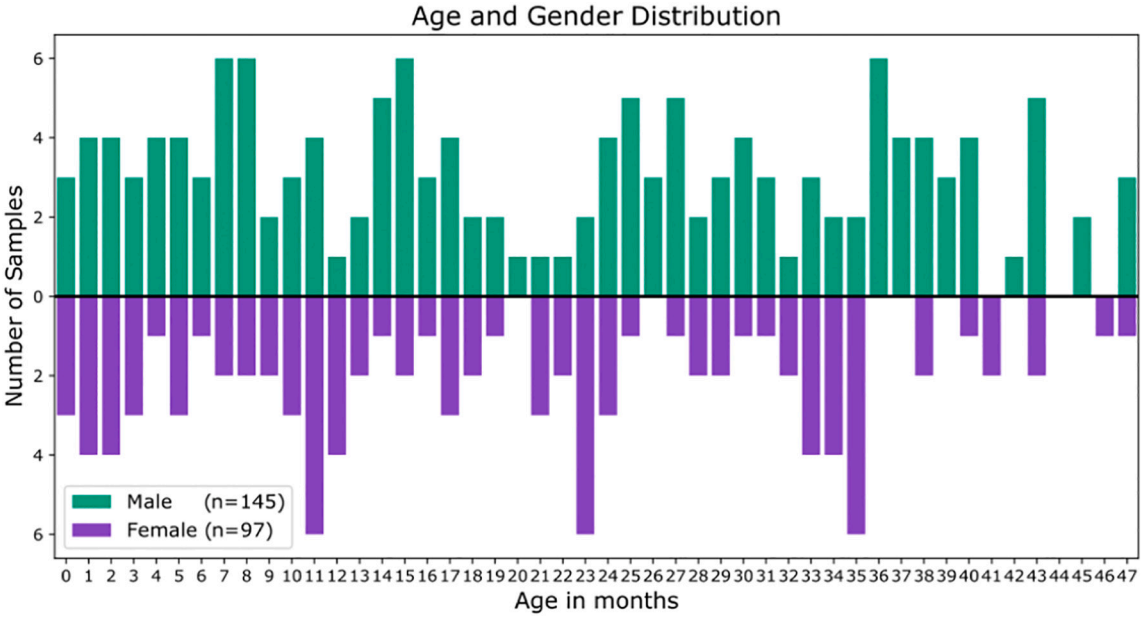

Fig. 1. Age and sex breakdown of the study population.

Booth et al., 2018; Knoops et al., 2019; Morice et al., 2020; Gao et al., 2020) with 3D morphable models (3DMM) being one of the more recent statistical shape models (Booth et al., 2016; Blanz and Vetter, 1999; Dai et al., 2017; Ploumpis et al., 2020; Dai et al., 2018; Zolfaghari et al., 2016; Khamis et al., 2015; Li et al., 2015). These craniofacial models have elucidated the potential usefulness for craniofacial surgery; however, normal models are lacking, especially for the facial skeleton. The mandible (lower jaw) is a complex bony structure of the face and is commonly affected in congenital craniofacial conditions. Examples include micrognathia (small mandible) in Robin sequence and (asymmetrical) mandibular hypoplasia in craniofacial microsomia. When a child is born with a mandibular malformation this can lead to numerous functional impairments, including airway obstruction, feeding impairment, and facial asymmetry (Claire Kane and Lauren, 2016).

Mandibular deformities and associated functional impairments have a highly variable phenotypic presentation, thus adequate evaluation of the deformity is essential for both diagnostic and therapeutic purposes. Classification and characterisation of mandibular anomalies are mainly based on qualitative criteria and 2D measurements (Swanson et al., 2016). However, a robust reference based on normative data is required in order to adequately assess deformity. Normative data has typically been studied using traditional (cephalometric) measurements and angles calculated by means of anatomical landmarks (Liu et al., 2010). Based on these studies, we know that a healthy growing mandible undergoes the greatest change in shape and size during the first year of life, including an increase in intercondylar width, ramus height, and corpus length (Liu et al., 2010; Smartt et al., 2005).

Recent studies on early mandibular development using 3D reconstructions of computed tomography (CT) scans are based on relatively small datasets (Liu et al., 2010; Hutchinson et al., 2012; Franklin et al., 2008; Hilger et al., 2003), primarily consider older age samples (Vallabh et al., 2020) or lack analysis of the complete mandibular shape (Karlo et al., 2010). In addition, most do not comprehensively capture 3D variation in shape and size due to usage of Euclidean distances and angles between anatomical landmarks (Schipper et al., 2021). For accurate understanding of 3D mandibular growth, a holistic shape analysis has been shown to be imperative (Morice et al., 2020; Krarup et al., 2005). Using modern geometric morphometrics this study aims to construct a 3D morphable model (3DMM) of the mandible for children under 4 years of age, asses its ability to capture early morphological variation of the mandible related to age and sex, and present growth curves for 3D anthropometric mandibular measurements.

2. Dataset and methods

2.1. The paediatric dataset

CT-scans of children aged 0–48 months at time of scan were collected

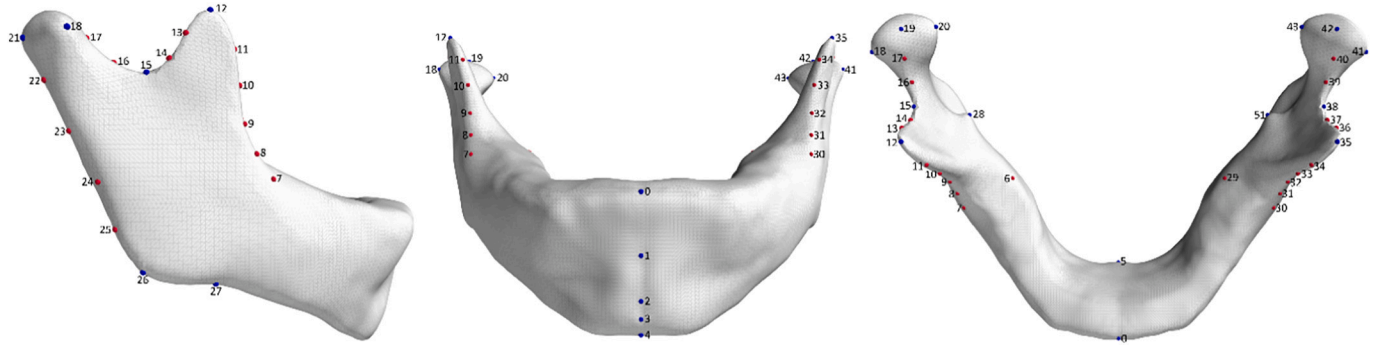

Fig. 2. Mandibular landmarks from lateral view, anterior view, and superior view (left to right). Validated landmarks are shown in dark blue and only these landmarks were used for rigid alignment. All landmarks were used to seed the NICP algorithm to achieve dense correspondence.

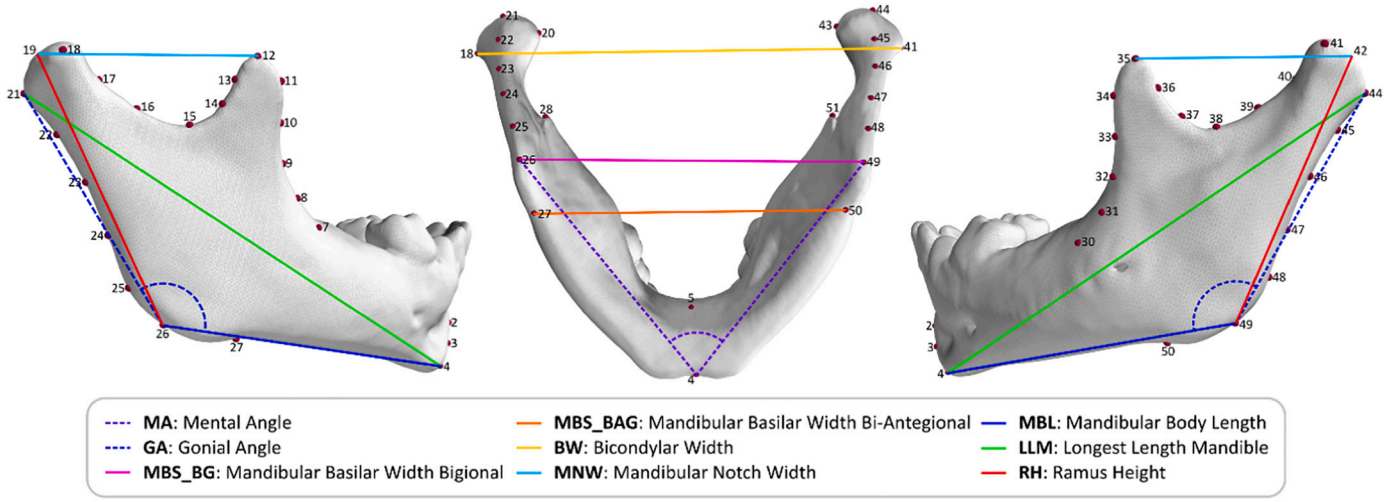

Fig. 3. Anthropometric measurements from right, inferior, and left perspectives.

at the Necker Children's Hospital, (Necker-Enfants Malades Hospital, NEMH), Paris, France. Scans were acquired for the years between 2011 and 2018. Only high-quality CT scans (>100 slices per scan and ≤1 mm per slice) of patients in the desired age range without anomalies visible on CT were included. All patients were informed of the study and notified on the use of their CT scan for scientific purposes. If a patient did not wish to be included, their scan was omitted from the data set. Scans were acquired for patients indicated for headache, trauma, or epilepsy and were assessed by two independent reviewers, a paediatric radiologist, and a clinical research fellow in craniofacial surgery (L.S.v.d.L.). Any scan presenting with abnormalities, craniofacial anomalies, or mandible fractures were excluded. Baseline characteristics were collected from corresponding medical charts. The final dataset consisted of CT scans from 242 children (59.9% male). The included patients had a mean age of 20.6 ± 13.4 months (median, 19.5 months). Mean ages for male and female samples were comparable (male: 21.3 ± 13.6 months, female: 19.5 ± 12.9 months, p = 0.3) (Fig. 1).

All DICOM-files were converted to 3D objects (mesh) by applying semi-automated thresholding techniques using a default bone setting, the mandible was then isolated from the skull with a foreground/background tool and saved as Object (.obj) file (software Mimics Imprint 3.0, Materialise, Leuven, Belgium). The mandibular canal and air pockets within the mandible were also removed, leaving only the outer surface of the mandible. A set of 52 validated and non-validated landmarks were used to annotate all isolated mandible meshes (Fig. 2, description in Supplementary Materials, software R3DS WRAP3D). Validated landmarks are those that correspond to defined anatomical positions (e.g.: infradentale, B-point, pogonion), whereas non-validated landmarks are those placed at equal intervals between validated landmarks (e.g.: landmarks 13 and 14 are placed at equal spacing between landmark 12, the right coronoid process, and landmark 15, the right mandibular notch). The meshes were put in dense correspondence with a mandible template mesh using the non-rigid iterative closest point algorithm (NICP) (Amberg et al., 2007). The template mesh was a watertight mesh consisting of ≈19k vertices and ≈38k faces in a fixed triangulation. Dentition was omitted from the mesh template. The full set of 52 landmarks was used to guide the NICP registration process. The processed mandible meshes were rigidly aligned to remove translation and rotation effects using the validated landmark subset, though size effects were retained during processing.

2.2. Landmark reliability

To assess landmark placement reliability, thirty meshes were randomly selected from the dataset to be landmarked for a second time by the initial annotator. An interval of at least three months was left between annotation sessions to minimise memory bias. Error means and standard deviations were then calculated for all landmarks.

2.3. Anthropometric measurements

Nine anthropometric lengths and angles were assessed (Fig. 3) (Hutchinson et al., 2012; Schipper et al., 2021). Measurement lengths were calculated using the standard distance formula:

$$distance = \sqrt{(x_A - x_B)^2 + (y_A - y_B)^2 + (z_A - z_B)^2}$$

where A and B are two distinct landmarks and x, y, and z are their coordinates in Cartesian space. To calculate the mental and gonial angle, the cosine rule was applied upon calculation of the measurements between the landmarks defining the angles. Then measurements were calculated for each of the samples in the dataset and compiled by 6-month age groups. Growth curves were plotted for male, female, and all individuals.

2.4. 3D morphable model

When all meshes had been put in dense correspondence, PCA was applied to the processed meshes to construct the 3DMM. The **compactness**, **generalisation**, and **specificity** of the 3DMM were evaluated. Compactness is defined as the percentage of the shape variance explained when a certain number of principal components are retained. Generalisation is a measure of the ability of the model to accurately represent novel shape samples not encountered during model training, while specificity evaluates the ability of the model to generate valid novel samples. The generalisation error was calculated as the average Euclidean distance (AED) between the unseen shape instance and the corresponding model representation. To calculate the AED, let A and B be two meshes with i vertices, where x, y, and z represent the Cartesian coordinates of each vertex. The AED can then be calculated on a per-vertex basis as follows:

$$AED = \frac{\sum_{i=1}^{n} \sqrt{\left(x_{i,A} - x_{i,B}\right)^2 + \left(y_{i,A} - y_{i,B}\right)^2 + \left(z_{i,A} - z_{i,B}\right)^2}}{n}$$

The generalisation error across the range of retained principal components is then given as the mean per-vertex error over all meshes. Model specificity was calculated by randomly synthesising 1000 random mandible samples at each of the model principal components following a multivariate normal distribution. For each synthesised mesh, the

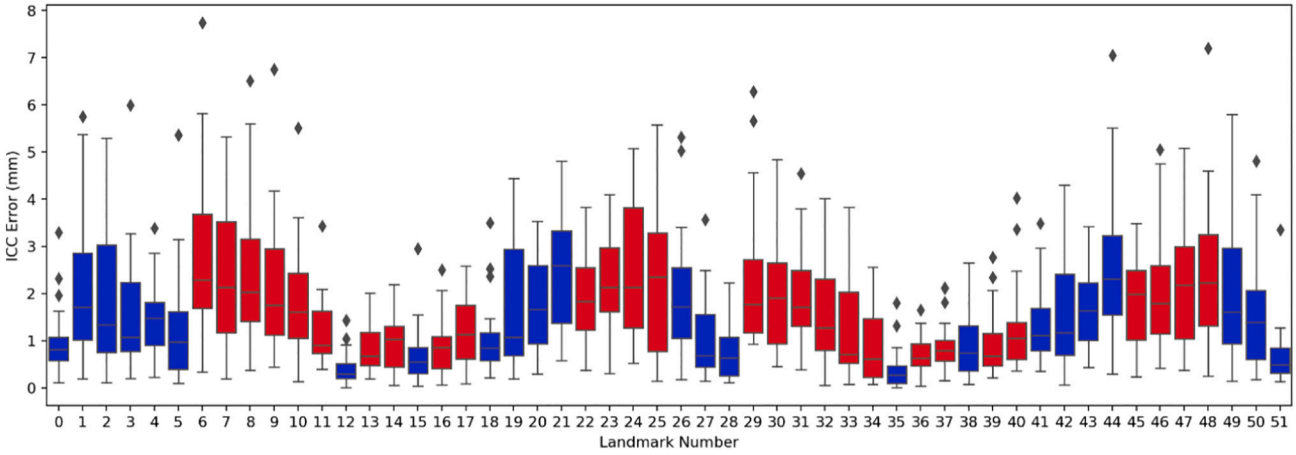

Fig. 4. Intra-rate landmark errors and standard deviations. Validated landmarks are shown in blue, and all other landmarks are shown in red.

specificity error was calculated as the AED over all mesh vertices between the synthesised mesh and its nearest neighbour in the test dataset. As a relatively small number of samples were used for the construction of the mandible model, both generalisation and specificity were evaluated using a leave-one-out strategy.

The mean 3DMM mandible shape was extracted and validated using the mean of the anthropometric measurements acquired from the population. The template validation process can be found in the supplemental materials.

2.5. *Partial least squares regression analysis*

Partial least squares (PLS) regression analysis was performed on the processed mandible meshes to assess how mandibular shape related to age and sex within the dataset.

The shape changes most associated with the age and sex were visualised by deforming the mean PLS shape template along the extracted shape modes. Ten shape modes were used in the construction of both age- and sex-based PLS models.

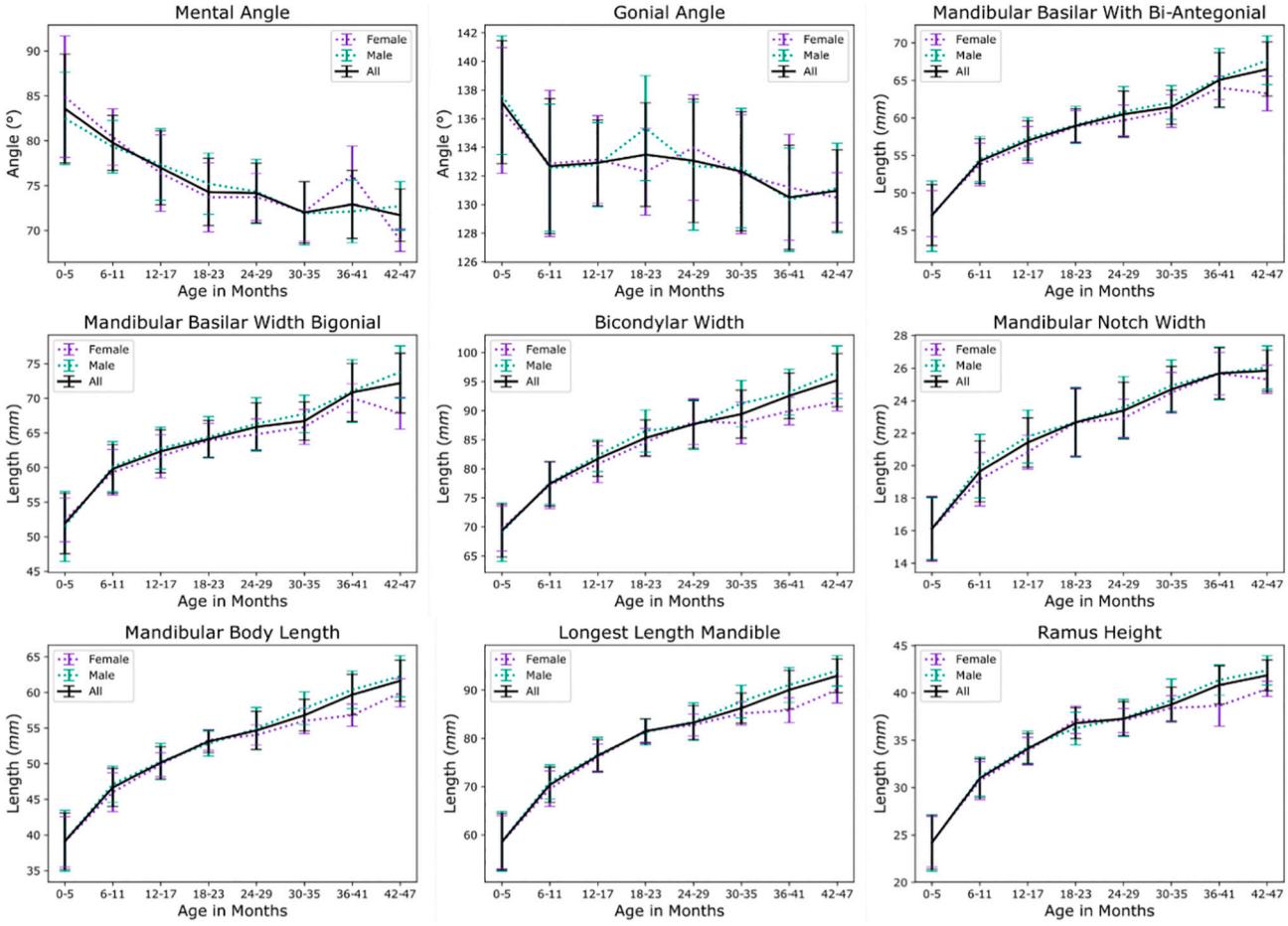

Fig. 5. Paediatric mandibular growth curves showing the mean and standard deviation for assessed lengths and measurements when patients were compiled by 6-month age groups.

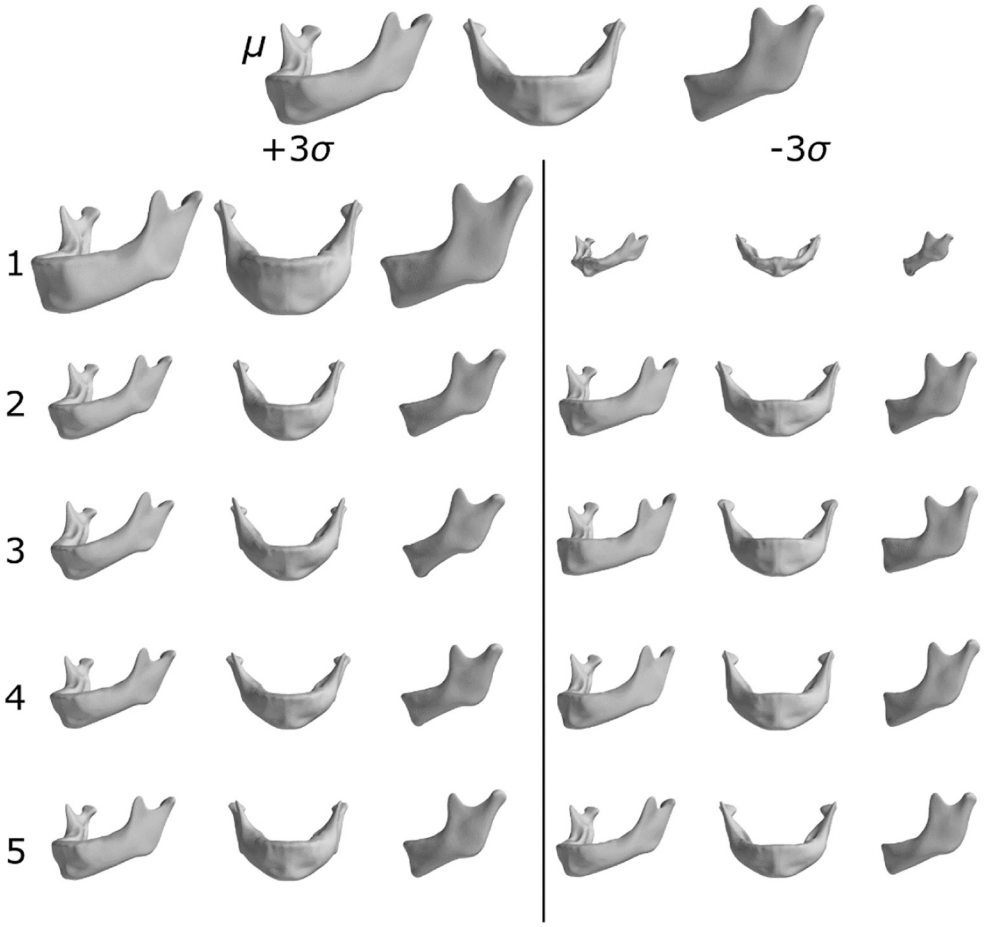

Fig. 6. Visualisation of the mandible 3DMM. The mean shape, μ, and the first five principal components are shown. The principal components are visualised as either an addition or a subtraction from the mean shape with a weight or ± 3σ, where σ_i is the standard deviation of the ith principal component. Each model instance is shown at a 45° angle, from a front perspective, and from a lateral perspective.

The relationship between the extracted PLS modes and subject age was assessed using a standard bi-variate correlation analysis. Spearman's R was used in all cases. The regressive nature of PLS was further employed to predict the age of a test set of subjects after the PLS model had been fitted to a training set. A 10-fold cross-validation schema was used, and a random stratified sampling strategy performed to define the folds. The R2 score and root mean square error (RMSE) were calculated to evaluate the prediction accuracy.

A similar strategy was employed to assess the association between extracted PLS shape modes and subject sex. A point-biserial correlation was used to assess the relationship between sex and extracted shape modes. Partial least square discriminant analysis (PLS-DA), the binary equivalent of PLS, was employed to facilitate model training and sex prediction. A 10-fold cross-validation schema with random stratified sampling was employed. Sex prediction accuracy and F1 scores were calculated.

The mean PLS mandible shape was extracted and validated using the population average of all assessed anthropometric measurements.

3. Results

3.1. Landmark reliability

Results of the intra-observer analysis are shown in Fig. 4. The mean error for most landmarks fell within 2 mm and all landmarks demonstrated an intra-observer error within 1.5 standard deviations of their respective means. Outliers were observed for 40 of the 1560 landmarks included in the analysis.

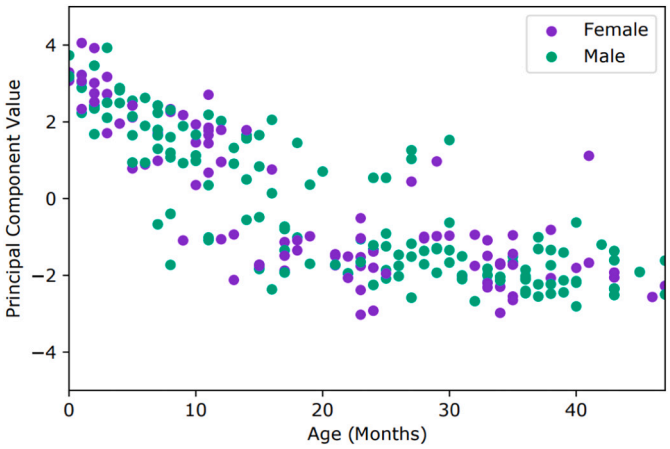

Fig. 7. Scatter plot of the first principal component by age labelled by sex. No clear sexual dimorphism is noted.

3.2. Anthropometric measurements

The mean mental angle and gonial angle were noted to decrease with age, while all measured lengths were shown to increase with patient age. No significant differences were observed between male and female subjects (Fig. 5). Mean and standard deviation for all assessed anthropometric measurements are reported in the supplemental materials.

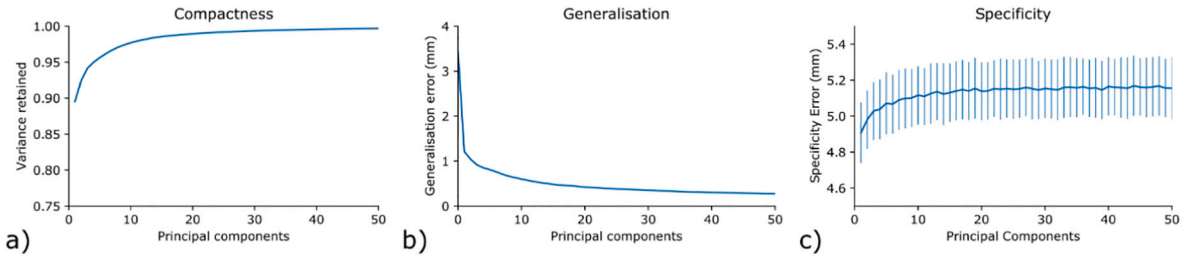

Fig. 8. a) Compactness, b) generalisation, and c) specificity of the paediatric mandible model.

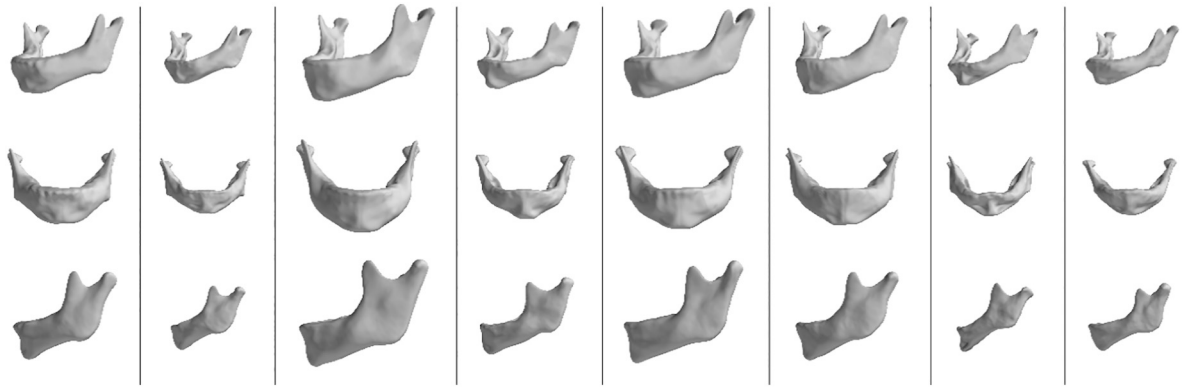

Fig. 9. Mandible samples generated from the mandible 3DMM using a multivariate Gaussian distribution.

3.3. 3D morphable model validation

The mean shape and the first five principal modes of shape variation are shown in Fig. 6. The first principal component is dominated by size effects and is highly correlated with age (Spearman's $r = 0.94$, $p < 0.01$). No distinct sexual dimorphism was noted with age along the principal mode of variation (Fig. 7). Variation in mandibular morphology along successive principal components, where scale is no longer a dominant factor, is shown in Fig. 6.

Besides the apparent size effects, from negative to positive extremes along the first principal component, an increased prominence of the anterior mandibular body with an increasing mandibular body length and narrowing of the mental angle is noted. In addition, the lower symphyseal border shows an increasingly anterior inclination and a relative narrowing of the inter-condylar width. Moreover, a larger ramus is apparent. For the second principal component, a narrowing of the inter-condylar width and a more acute gonial angle are observed. The third principal component demonstrates a change in the gonial angle from obtuse to acute and a less prominent condyle relative to the coronoid process. For the fourth and fifth principal component, both of which represent less than 1% of explained variance, the shape changes from negative to positive extremes are less evident, but include a larger anteroposterior ramus width and a slight narrowing of the mental angle.

Fig. 8a demonstrates that the model is sufficiently compact. Almost 90% of the shape variance is captured within the first principal component alone, and over 99% of the total shape variance within the dataset is captured within the first 22 model components. The model is also seen to generalise well to unseen instances, with a mean generalisation error of less than 0.5 mm when 15 more principal components are used (Fig. 8b). This decreases to 0.17 mm when 160 components are used. The mean specificity error is 5.1 mm when 160 principal components are used (Fig. 8c). While the specificity error reported here is relatively high, the size of this value can be attributed to the inclusion of size in the model and the relatively small number of samples used in the model construction. Fig. 9 shows diverse range of the mandible samples generated using our model. All represent plausible mandibles, indicating that the model is indeed capable of generating realistic shape samples.

3.4. Partial least squares analysis – covariance with age and sex

PLS analysis demonstrates significant correlations between the extracted PLS shape modes and age at time of scan. The shape variations along the three most highly correlated shape modes are shown in Fig. 10. As with PCA, the first extracted PLS mode captures much of the size variation within the dataset and is highly correlated with age (Fig. 11a, $r = -0.9$, $p < 0.01$). The correlation between all PLS shape modes and age is given in Table 1. The application of the age based PLS regression model for age prediction yielded an R2 score of 0.94 and an RMSE of 3.3 months when 10 PLS shape modes were used. The correlation between predicted age and true age in months is shown in Fig. 11b.

Extracted PLS shape modes associated with sex, as shown in Fig. 10, are visually similar to those of the age-based model. The correlation between extracted shape modes and sex is low in all cases (Table 2). The accuracy of the PLS-DA model for sex prediction achieved an F1-Score of 71.7% and an accuracy of 65.7% when 10 PLS shape modes were included (Fig. 11c). While this is higher than the maximum chance accuracy of 59.9% (the percentage of patients that are male), the dataset is unbalanced in both age and sex. Combining this with the uninformative visualisation of the extracted gender-based components, it is unlikely that any true sex-based shape changes have been extracted (Fig. 11).

4. Discussion

The use of geometric morphometrics allowed for construction of a comprehensive 3DMM of the mandible for a normative population between 0 and 4 years of age. The high correlation between the first principal component and age indicates a significant allometric component for mandibular shape variation in this population (Spearman's $r = 0.94$, $p < 0.01$) with 89.5% of the shape variance captured along this component. The majority of this variance can be attributed to mandible size. In line with this finding, the model showed a high correlation

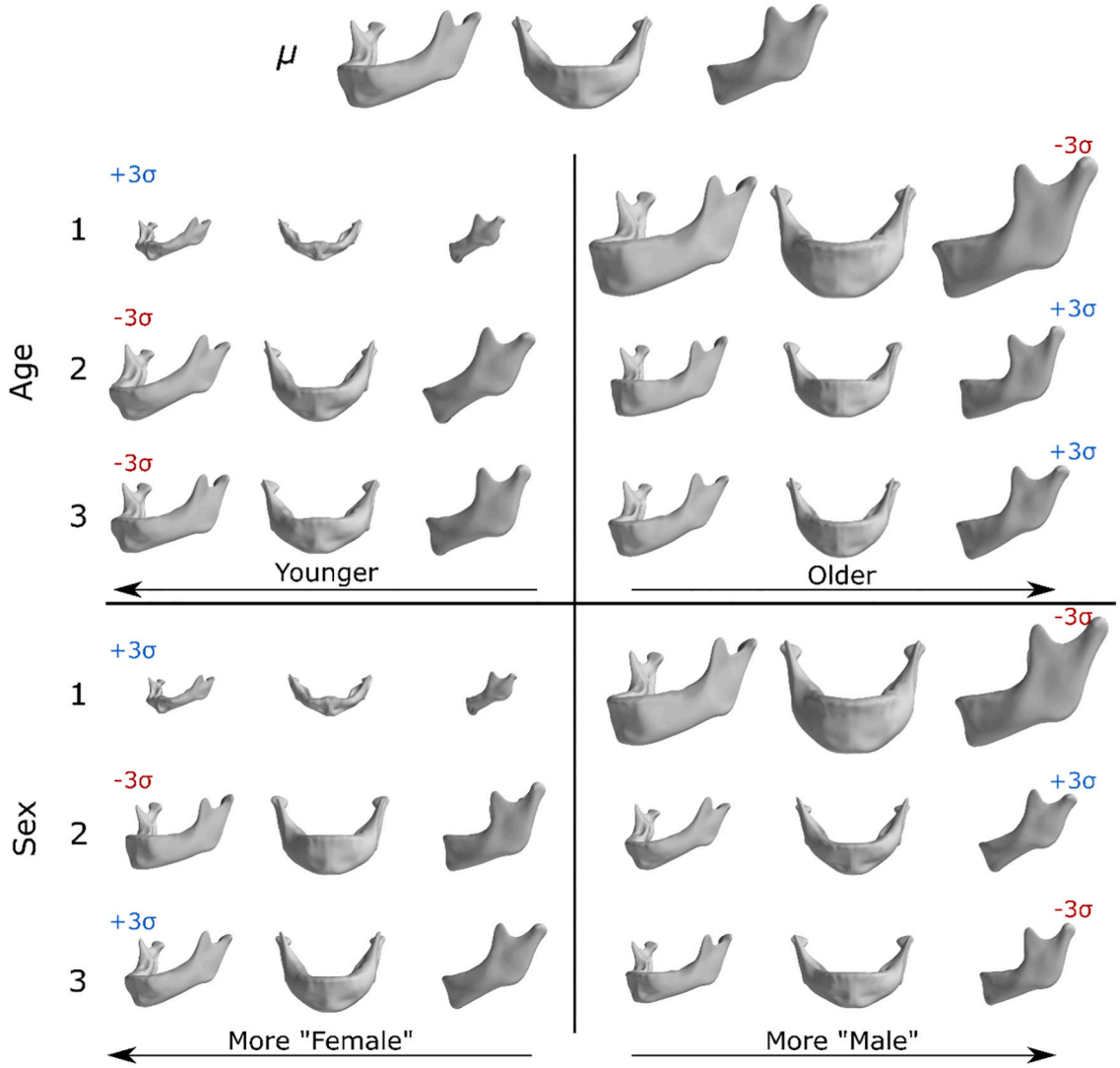

Fig. 10. Visualisation of the first three extracted PLS shape modes for the age-based (top) and sex-based (bottom) PLS models. The mean shape, μ, and the first three shape modes are shown. Each model instance is shown at a 45° angle, from a front perspective, and from a lateral perspective.

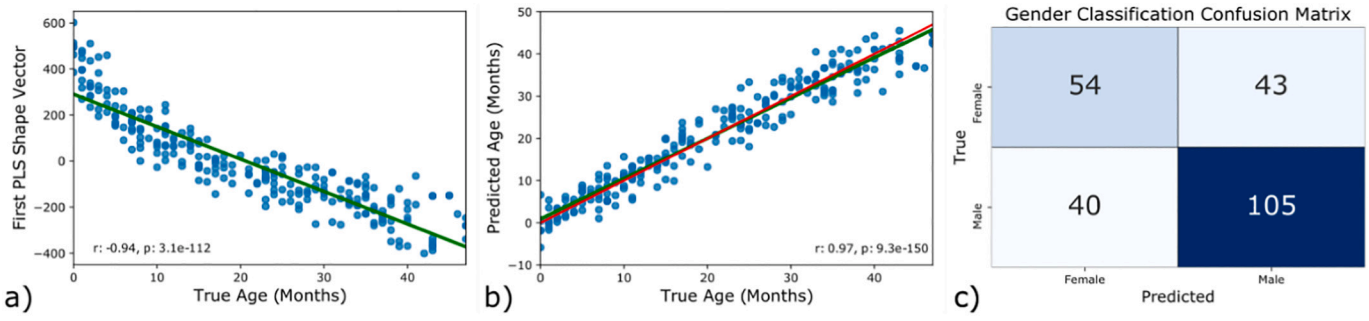

Fig. 11. a) Correlation between the first component of the age-based PLS model and true age. The green line indicates the line of best fit. b) Correlation between predicted age and true age regressed from the age-based PLS model using a 10-fold cross validation. The green line indicates the line of best fit, and the red line is the line of equality (perfect prediction). c) Confusion matrix for sex classification using the sex-based PLS model with 10-fold cross validation. Spearman's R and corresponding p-value are shown in the bottom corners of a) and b).

between the predicted age and true age based on the shape modes extracted using PLS regression analysis (Spearman's $r = 0.97$, $p < 0.01$). This is further reflected in the change of anthropometric measurements with age. For sex, variation in mandibular shape was less evident, with lower correlation coefficients between sex and shape modes in the PLS regression analysis. In addition, an accuracy of 65.7% for sex classification was noted, only marginally better than the chance classification accuracy of 60%. As the dataset is unbalanced in terms of both age and sex, however, it is unlikely that any accuracy gains are due to sex-based shape changes. This is in line with the lack of a significant difference in

Table 1
Spearman's correlation coefficient for the successive PLS shape modes (SM) and subject age.

	SM 1	SM 2	SM 3	SM 4	SM 5	SM 6	SM 7	SM 8	SM 9	SM 10
R	−0.938	0.224	0.194	0.148	−0.056	0.068	−0.063	−0.034	0.064	−0.067
P	<0.001	<0.001	0.002	0.021	0.388	0.290	0.329	0.598	0.324	0.301

Table 2
Point biserial correlation coefficient for the successive PLS shape modes (SM) and subject sex.

	SM 1	SM 2	SM 3	SM 4	SM 5	SM 6	SM 7	SM 8	SM 9	SM 10
R	−0.15	0.23	−0.24	−0.24	−0.29	−0.23	−0.24	0.214	−0.16	−0.21
P	0.019	<0.001	<0.001	<0.001	<0.001	<0.001	<0.001	0.001	0.014	0.001

the anthropometric measurements between male and female patients, a finding that is supported in the literature for a paediatric population (Hilger et al., 2003; Stunz, 1941; Franklin et al., 2007; Kelly et al., 2017). Although PLS shape modes did show a statistically significant different between males and females, the observed correlations were small and combining successive PLS modes did not lead to a substantial predictive value for males and females. This observation in line with the sexual dimorphism described by Coquerelle et al. (2013) who noted that sex-based shape differences are small when compared with age-based differences.

Previous geometric morphometric studies of early mandibular development have primarily used anatomical landmark coordinates only (Liu et al., 2010; Hutchinson et al., 2012; Hilger et al., 2003). In contrast, the methods used in this study provide a particularly comprehensive description of mandibular shape variation in the growing child, which provides much more information. Using a statistical approach, the morphological changes in early mandibular shape development were highlighted and are mainly associated with an allometric scaling of the mandible, i.e. non-proportional size changes. From negative to positive extremes along the first principal component, an increasing prominence is noted for the anterior mandibular body with an increasing mandibular body length and narrowing of the mental angle. In addition, the lower symphyseal border shows an increasingly anterior inclination, in concurrence with the labial unrolling described by Coquerelle et al. (2013). Similarly, the gonial angle grows more acute and the condyle grows more prominent than the coronoid process. While spanning a larger age range with fewer samples, the geometric morphometric shape deformations of landmark coordinates along the first principal component shown by Franklin et al. are similar to those found here (Franklin et al., 2008).

The mandibular shape variations along the principal component axes are reflected in the cross-sectional anthropometric measurements. Growth curves for clinically pertinent anthropometric measurements were obtained using 3D linear measurements between landmarks and angulations. Schipper et al. reported an increase in mandibular body length and ramus height for children between 0 and 2 years of age with a decline in rate of growth after the first year of life (Schipper et al., 2021). While also true for our study, persistent growth was observed up to 4 years of age. In contrast, no decline and subsequent increase in the rate of growth for the mandibular body was noted in our study, but rather consistent growth. The bigonial and bicondylar width showed similar growing trends with a relatively larger increase in the latter compared to the former noted here. Franklin et al. reported similar findings for the gonial angle and mental angle with a more obtuse gonial and mental angle for younger dry mandible specimens (Franklin et al., 2008). Klop and Amsterdam also created a 3D morphable model of the growing mandible from anonymous dry mandible specimens estimated to be between 1 and 12 years old with similar results (Klop and Amsterdam, 2021).

The measures presented in our results, including shape deformations and anthropometric measures, are implicated in various clinical contexts. Mandibular morphology represents an accurate predictor of age, in line with previous reports (Franklin et al., 2008). This is largely related to concurrent dental development, which was excluded from our model, and functional anatomical changes with age (Remy et al., 2019). Furthermore, some degree of sexual dimorphism was noted for the mandible for the included age range. The anthropometric growth curves presented here can be used as reference values for clinical purposes, e.g. follow-up of growth or operative planning purposes, in the case of children with an underdeveloped lower jaw undergoing mandibular distraction osteogenesis. The detailed description of early mandibular shape variation allows for comparison of mandibular morphology with developmental conditions in which the mandible is affected, e.g. Robin sequence, Nager, and Treacher Collins syndrome. Applications could include automated shape analyses and assisting in more accurate characterisation of mandibular deformities when compared to an unaffected population. This could help inform distraction vectors and evaluate operative results, i.e. to what extent mandibular shape was normalised. Moreover, this model has potential applications within forensic sciences to help identify age of a person based on the mandibular shape.

The presented model has demonstrated strong intrinsic characteristics, however, there are several limitations. First, the use of cross-sectional data only allows for a population average to be derived for anthropometric measurements over time. Similarly, while an association of early mandibular shape variation with age is described, the use of cross-sectional data does not allow for an exact description of how this may develop for individual patients. The lack of longitudinal CT-imaging data for a normal population is primarily due to evident ethical reasons related to radiation exposure. That said, the presented dataset, which was constructed from 242 distinct samples, represents the largest set of three-dimensional mandibular shape reconstructions for the studied age group. The resulting 3DMM was shown to be capable of reliably synthesising novel mandible instance, which may prove beneficial in future applications as an alternative to limited data. As such, a comprehensive range of normal values for both anthropometric mandibular measurements and mandibular shape representations for various ages can be obtained.

Future studies could also evaluate the mandibular shape and functional problems, such as airway difficulties. This could be of use in disorders where multiple organs might be in play and understanding of associations between shape abnormalities and severity of symptoms could guide the treatment plan. In addition, further expanding the data population to adulthood would allow for construction of an increasingly comprehensive normative mandibular model.

In conclusion, a 3DMM was constructed to describe early mandibular shape variation for a normative population between the ages of 0–4 years. We applied an existing pipeline to evaluate the mandibular shape comprehensively. The model has applications for assessment of mandibular deformities and might improve diagnostic accuracy for craniofacial conditions that impact mandibular morphology. Further applications include surgical planning and objective surgical outcomes evaluation, and patient follow-up, which might benefit from the early

growth curves provided in this study.

CRediT authorship contribution statement

Ms. Eimear O' Sullivan contributed to the conception, design, analysis, and interpretation of the data, writing and revision of the manuscript.

Dr. Lara S. van de Lande contributed to the conception, design, acquisition and analysis of the data, interpretation of the data, writing and revision of the manuscript.

Dr. Khalid El Ghoul, contributed to the design, acquisition and interpretation of the data, and writing and revision of the manuscript.

Ass.Prof.. Maarten J. Koudstaal, contributed to the design, interpretation of the data and critical analysis of the manuscript.

Prof. Roman H. Khonsari contributed to the data acquisition and critical analysis of the manuscript.

Prof. Silvia Schievano, Prof. David J. Dunaway, and Prof. Stefanos Zafeiriou contributed to the conception, design, interpretation of the data, and critical analysis of the manuscript.

Declaration of competing interest

We declare no competing interests.

Acknowledgements

This research was supported by Great Ormond Street Hospital for Children's Charity through the FaceValue programme grant (no. 508857), the Engineering and Physical Sciences Research Council (EP/N02124X/1) and the European Research Council (ERC-2017-StG-757923). This work was undertaken at GOSH/ICH, UCLH/UCL who received a proportion of funding from the United Kingdom Department of Health's NIHR Biomedical Research Centre funding scheme. The funders had no role in study design, collection, analysis and interpretation of the data, decision to publish, or preparation of the manuscript.

Appendix A. Supplementary data

Supplementary data to this article can be found online at https://doi.org/10.1016/j.bonr.2022.101528.

References

Amberg, B., Romdhani, S., Vetter, T., 2007. Optimal step nonrigid ICP algorithms for surface registration. In: 2007 Ieee Conference on Computer Vision and Pattern Recognition, Vols 1-8, 1491-+.

Blanz, V., Vetter, T., 1999. A morphable model for the synthesis of 3D faces. In: Proceedings of the 26th Annual Conference on Computer Graphics and Interactive Techniques, pp. 187–194.

Booth, J., Roussos, A., Zafeiriou, S., Ponniah, A., Dunaway, D., 2016. A 3d morphable model learnt from 10,000 faces. In: Proceedings of the IEEE Conference on Computer Vision and Pattern Recognition, pp. 5543–5552.

Booth, J., Roussos, A., Ponniah, A., Dunaway, D., Zafeiriou, S., 2018. Large scale 3d morphable models. Int. J. Comput. Vis. 126, 233–254.

Claire Kane, M., Lauren, L.M., 2016. In: Feeding and Swallowing Issues in Infants With Craniofacial Anomalies. Perspectives of the ASHA Special Interest Groups, 1, pp. 13–26.

Coquerelle, M., Prados-Frutos, J.C., Benazzi, S., Bookstein, F.L., Senck, S., Mitteroecker, P., Weber, G.W., 2013. Infant growth patterns of the mandible in modern humans: a closer exploration of the developmental interactions between the symphyseal bone, the teeth, and the suprahyoid and tongue muscle insertion sites. J. Anat. 222, 178–192.

Dai, H., Pears, N., Smith, W.A., Duncan, C., 2017. A 3d morphable model of craniofacial shape and texture variation. In: Proceedings of the IEEE International Conference on Computer Vision, pp. 3085–3093.

Dai, H., Pears, N., Smith, W., 2018. A data-augmented 3D morphable model of the ear. In: 2018 13th IEEE International Conference on Automatic Face & Gesture Recognition (FG 2018). IEEE, pp. 404–408.

Franklin, D., Oxnard, C.E., O'Higgins, P., Dadour, I., 2007. Sexual dimorphism in the subadult mandible: quantification using geometric morphometrics. J. Forensic Sci. 52, 6–10.

Franklin, D., Cardini, A., O'Higgins, P., Oxnard, C.E., Dadour, I., 2008. Mandibular morphology as an indicator of human subadult age: geometric morphometric approaches. Forensic Sci. Med. Pathol. 4, 91–99.

Gao, Z., Chen, Y., Li, F., Li, H., Liu, J., Wu, W., Hao, J., Wang, H., 2020. A novel geometric morphometric analytical method for classifying mandibular morphology in infants with isolated Pierre Robin sequence. J. Oral Maxillofac. Surg. 78 (822) pp. e1–822. e16.

Hilger, K.B., Larsen, R., Wrobel, M.C., 2003. Growth modeling of human mandibles using non-euclidean metrics. Med. Image Anal. 7, 425–433.

Hutchinson, E.F., L'Abbé, E.N., Oettle, A.C., 2012. An assessment of early mandibular growth. Forensic Sci. Int. 217 (233) pp. e1–233. e6.

Karlo, C.A., Stolzmann, P., Habernig, S., Müller, L., Saurenmann, T., Kellenberger, C.J., 2010. Size, shape and age-related changes of the mandibular condyle during childhood. Eur. Radiol. 20, 2512–2517.

Kelly, M.P., Vorperian, H.K., Wang, Y., Tillman, K.K., Werner, H.M., Chung, M.K., Gentry, L.R., 2017. Characterizing mandibular growth using three-dimensional imaging techniques and anatomic landmarks. Arch. Oral Biol. 77, 27–38.

Khamis, S., Taylor, J., Shotton, J., Keskin, C., Izadi, S., Fitzgibbon, A., 2015. Learning an efficient model of hand shape variation from depth images. In: Proceedings of the IEEE Conference on Computer Vision and Pattern Recognition, pp. 2540–2548.

Klop, C., Amsterdam, M., 2021. A three-dimensional statistical shape model of the growing mandible. Sci. Rep. 11, 18843.

Knoops, P.G., Papaioannou, A., Borghi, A., Breakey, R.W., Wilson, A.T., Jeelani, O., Zafeiriou, S., Steinbacher, D., Padwa, B.L., Dunaway, D.J., 2019. A machine learning framework for automated diagnosis and computer-assisted planning in plastic and reconstructive surgery. Sci. Rep. 9, 1–12.

Krarup, S., Darvann, T.A., Larsen, P., Marsh, J.L., Kreiborg, S., 2005. Three-dimensional analysis of mandibular growth and tooth eruption. J. Anat. 207, 669–682.

Li, Z., Park, B.-K., Liu, W., Zhang, J., Reed, M.P., Rupp, J.D., Hoff, C.N., Hu, J., 2015. A statistical skull geometry model for children 0–3 years old. PLoS One 10, e0127322.

Liu, Y.-P., Behrents, R.G., Buschang, P.H., 2010. Mandibular growth, remodeling, and maturation during infancy and early childhood. Angle Orthod. 80, 97–105.

Morice, A., Cornette, R., Giudice, A., Collet, C., Paternoster, G., Arnaud, É., Galliani, E., Picard, A., Legeai-Mallet, L., Khonsari, R., 2020. Early mandibular morphological differences in patients with FGFR2 and FGFR3-related syndromic craniosynostoses: a 3D comparative study. Bone 141, 115600.

E O'Sullivan LS van de Lande A Papaioannou RW Breakey NO Jeelani A Ponniah C Duncan S Schievano RH Khonsari S Zafeiriou . Craniofacial Syndrome Identification Using Convolutional Mesh Autoencoders. Available at SSRN 3795325.

Ploumpis, S., Ververas, E., O'Sullivan, E., Moschoglou, S., Wang, H., Pears, N., Smith, W., Gecer, B., Zafeiriou, S.P., 2020. Towards a complete 3D morphable model of the human head. IEEE Trans. Pattern Anal. Mach. Intell. 43 (11), 4142–4160.

Remy, F., Godio-Raboutet, Y., Captier, G., Burgart, P., Bonnaure, P., Thollon, L., Guyot, L., 2019. Morphometric characterization of the very young child mandibular growth pattern: what happen before and after the deciduous dentition development? Am. J. Phys. Anthropol. 170, 496–506.

Schipper, J.A.M., van Lieshout, M.J., Böhringer, S., Padwa, B.L., Robben, S.G., van Rijn, R.R., Koudstaal, M.J., Lequin, M.H., Wolvius, E.B., 2021. Modelling growth curves of the normal infant's mandible: 3D measurements using computed tomography. Clin. Oral Investig. 1–11.

Smartt Jr., J.M., Low, D.W., Bartlett, S.P., 2005. The pediatric mandible: I. A primer on growth and development. Plast. Reconstr. Surg. 116, 14e–23e.

Stunz, D.I., 1941. The mandibular angle in infancy: its significance and modification. J. Am. Dent. Assoc. 28, 921–928.

Swanson, J.W., Mitchell, B.T., Wink, J.A., Taylor, J.A., Bartlett, S.P., 2016. Surgical classification of the mandibular deformity in craniofacial microsomia using 3-dimensional computed tomography. Plast. Reconstr. Surg. Glob. Open 4, e598.

Vallabh, R., Zhang, J., Fernandez, J., Dimitroulis, G., Ackland, D.C., 2020. The morphology of the human mandible: a computational modelling study. Biomech. Model. Mechanobiol. 19.

Zolfaghari, R., Epain, N., Jin, C.T., Glaunes, J., Tew, A., 2016. Generating a morphable model of ears. In: 2016 IEEE International Conference on Acoustics, Speech and Signal Processing (ICASSP). IEEE, pp. 1771–1775.